



Deformation of charge density activated by conductive carbon with the piezoelectric effect of tourmaline for highly promoting $\text{Fe}^{3+}/\text{Fe}^{2+}$ cycle in Fenton-like process

Yingshi Zhu ^{a,b}, Jianqiu Zhu ^b, Huabin ShenTu ^c, Yanfei Wei ^b, Jun Wei ^c, Lecheng Lei ^{a,d}, Yuru Li ^b, Tao Yu ^b, Zhongjian Li ^{a,d}, Yang Hou ^{a,d,*}, Bin Yang ^{a,d,*}

^a Key Laboratory of Biomass Chemical Engineering of Ministry of Education, College of Chemical and Biological Engineering, Zhejiang University, Hangzhou 310058, China

^b Zhejiang Environment Technology Co., Ltd., Hangzhou 311100, China

^c Power China Huadong Engineering Co., Ltd., Hangzhou 311112, China

^d Institute of Zhejiang University-Quzhou, Quzhou 324000, China



ARTICLE INFO

Keywords:
Tourmaline
Conductive carbon
Electron transfer
 Fe^{3+} reduction
Fenton process

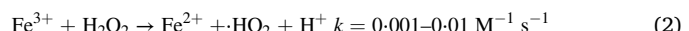
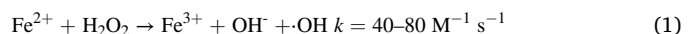
ABSTRACT

A novel Fe_3O_4 coated conductive carbon modified tourmaline ($\text{Tml@C@Fe}_3\text{O}_4$) catalyst with the nuclear shell structure was prepared to boost the $\text{Fe}^{3+}/\text{Fe}^{2+}$ cycle in Fenton-like process. The catalyst was prepared by a simple combination of hydrothermal method and calcination. The results showed that the smaller size of Tml in the core was beneficial to get the stronger piezoelectric effect. The reduction efficiency of Fe^{3+} for Tml@C was highly boosted by the deformation of charge density, and the optimum was 10.24 times of that before modification with an average size of 1.3 μm . Furthermore, the embedded layer of conductive carbon can also reduce iron leaching and shrink ultimate pH variation. The removal efficiencies of sulfathiazole (STZ) were 72.82–100 % at pH 3–7 in the present work. Therefore, this study provides a novel Fenton-like catalyst for the efficient treatment of antibiotics at a wide pH range.

1. Introduction

Antibiotics are widely used in the medical and livestock industries, resulting in massive annual use and emissions [1] and thus they have been detected in sewage treatment plants, surface water, groundwater, and soil [2]. Among them, sulfonamides are ubiquitous in aquatic environment, with the concentration ranging from ng L^{-1} to \mu g L^{-1} [3]. Especially, antibiotics can cause flora imbalances, allergic reactions and the development of drug-resistant bacteria and resistance genes [4]. Therefore, efficient methods have been adopted to handle the removal of antibiotics in water. Advanced oxidation processes, which can generate free radicals such as $\cdot\text{OH}$ and $\cdot\text{SO}_4^{2-}$, were often used in treating antibiotics in water [5,6]. Generally, the Fenton process is one of the most common methods used in practice, because it can disrupt the molecular structure of antibiotics and then their biotoxicity can be significantly reduced [7,8]. H_2O_2 is catalyzed by Fe^{2+} to produce $\cdot\text{OH}$ radicals (Eq. 1, $k = 40\text{--}80 \text{ M}^{-1} \text{ s}^{-1}$) with strongly oxidizing property in Fenton reaction,

and however the generated Fe^{3+} was difficult to be further reduced to Fe^{2+} by H_2O_2 owing to the slow reaction rate of only $0.001\text{--}0.01 \text{ M}^{-1} \text{ s}^{-1}$ (Eq. 2) [9]. In particular, much stricter operating conditions for conventional Fenton reaction should be fulfilled, where pH were usually set at 3, and thus it resulted in substantial dissolving of iron and a large quantity of waste sludge was formed [10,11].



Promoting $\text{Fe}^{3+}/\text{Fe}^{2+}$ cycling is a key challenge and hot spot in current research, which can continually catalyze the formation of $\cdot\text{OH}$ from H_2O_2 [12,13]. Generally, the $\text{Fe}^{3+}/\text{Fe}^{2+}$ cycle is promoted by adding reducing agents (e.g. ascorbic acid, gallic acid, cysteine, etc.) [14–16]. However, the addition of reducing agents may cause secondary contamination. Carbon materials have good electrical conductivity and can act as electron donors, so researchers have used them to promote

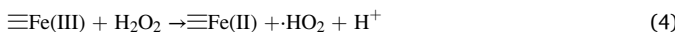
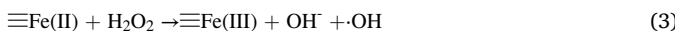
* Corresponding author at: Key Laboratory of Biomass Chemical Engineering of Ministry of Education, College of Chemical and Biological Engineering, Zhejiang University, Hangzhou 310058, China.

E-mail address: keyangb@zju.edu.cn (B. Yang).

Fe^{3+} reduction [17,18]. Cao et al. [19] prepared triethanolamine-/graphene oxide@ Fe_3O_4 -like Fenton catalysts, in which the off-domain π -electrons of graphene oxide and the lone pair of electrons of triethanolamine and its oxidation products promoted the regeneration of Fe^{2+} . Tang et al. [20] found that high-temperature derived biochar could transfer electrons to Fe^{3+} due to its edge defects and electrical conductivity. However, the reduction efficiency of Fe^{3+} in the above-mentioned literature was as low as less than 5%, when only carbon was used as the electron donor.

To address this, extra energy (e.g., electricity, light, ultrasound, etc.) was applied to enhance the reduction of Fe^{3+} to Fe^{2+} [21–23]. The utilization of electric fields generated by piezoelectric materials to promote $\text{Fe}^{3+}/\text{Fe}^{2+}$ cycle is a solution. In our previous study the electric field formed by tourmaline (Tml) under mechanical stress could drive the reduction of Fe^{3+} to Fe^{2+} [24]. However, the reduction efficiency of Fe^{3+} was low since electrons came from the electrolysis of OH^- . In addition, Li et al. [25] demonstrated that electron-rich conductive carbon materials can enhance the piezoelectric properties of piezoelectric materials by increasing the material conductivity. Therefore, a core-shell structure with Tml as the core and conductive carbon as the shell needs to be constructed to enhance the piezoelectric effect and electron transfer.

In addition, to get rid of the pH limitation, the researchers prepared heterogeneous catalysts to replace the direct injection of Fe^{2+} [26,27]. As shown in Eq. (3) and Eq. (4), H_2O_2 decomposition catalyzed directly by the active site at the catalyst interface [28,29]. Fe_3O_4 is commonly used as a Fenton catalyst to catalyze the formation of $\cdot\text{OH}$ from H_2O_2 , but it cannot reduce interfacial or dissolved ferric iron, requiring an additional electron donor to regenerate to ferrous iron.



In the present work study, a novel Fe_3O_4 coated conductive carbon modified tourmaline ($\text{Tml@C@Fe}_3\text{O}_4$) catalyst with the nuclear shell structure was prepared where conductive carbon was embedded between Tml and Fe_3O_4 for promoting the $\text{Fe}^{3+}/\text{Fe}^{2+}$ cycle. Firstly, the effect of the piezoelectric effect on Fe^{3+} reduction was investigated by using Tml of different particle sizes as substrates. Secondly, the reduction of Fe^{3+} at the catalyst interface was enhanced by modifying the Tml surface with different levels of conductive carbon, which was used as an electron donor. The catalyst surface morphology, crystalline structure, elemental content and electrochemical properties were characterized, and the density functional theory calculation was used to elucidate the mechanism by which the catalyst promotes Fe^{3+} reduction. Finally, Fe_3O_4 was further loaded onto the carbon-modified Tml surface, and the catalyst was used as a Fenton-like catalyst to remove sulfathiazole (STZ, a typical sulfonamide antibiotic contaminant) in the Fenton-like system and to investigate the degradation mechanism and pathway.

2. Materials and methods

2.1. Preparation of catalysts

The reagents and materials used in this study are listed in Text S1.

2.1.1. Preparation of Tml@Cx ($x = 1, 2, 3$)

The preparation method of Tml@Cx ($x = 1, 2, 3$) is shown in Fig. 1, and the specific method is as follows: (I) a certain amount of glucose and Tml with a mass ratio of (1–3): 3 were mixed well and added to a certain amount of ultrapure water and then stirred magnetically for 30 min; (II) the mixture was poured into a 100 mL reaction kettle and carried out a hydrothermal reaction at 160 °C for 12 h; (III) the product was washed with ultrapure water and ethanol twice; (IV) the product was filtered and dried at 80 °C for 12 h; (V) the dried product was placed in a quartz glass tube in a vacuum tube furnace and heated to 500 °C at a heating rate of 5 °C min⁻¹ and then held for 2 h. Tml with conductive carbon on the surface was finally produced. Among them, the prepared Tml@C catalysts were named Tml@C1 , Tml@C2 , and Tml@C3 according to the mass ratio of glucose and Tml.

2.1.2. Preparation of $\text{Tml@C@Fe}_3\text{O}_4$

The methods for $\text{Tml@C@Fe}_3\text{O}_4$ preparation are as follows: (I) a certain amount of glucose and Tml (mass ratio equal to Tml@Cx , which has the strongest reducing ability of Fe^{3+}) were mixed well and added to a certain amount of ultrapure water then stirred magnetically for 30 min; (II) a certain amount of $\text{FeCl}_2 \cdot 4 \text{H}_2\text{O}$, $\text{FeCl}_3 \cdot 6 \text{H}_2\text{O}$ and sodium citrate were added into the aforementioned mixture and continued to be stirred for 20 min. The remaining hydrothermal reaction and high temperature carbonization conditions were the same as that in Section 2.1.1.

2.2. Experimental setup

2.2.1. Fe^{3+} reduction experiment

The prepared 0.3 g of catalyst was added to 100 mL of ultrapure water at pH 3 and stirred at 300 rpm with an aeration rate of 400 mL min⁻¹ of N_2 to avoid the oxidation of Fe^{2+} . A further 300 $\mu\text{mol L}^{-1}$ Fe^{3+} was added and stirring was continued for 60 min before the Fe^{2+} concentration in the solution was measured. The control group was only stirred by N_2 aeration and no additional Fe^{3+} was added. The amount of Fe^{3+} reduced by the catalyst was calculated by subtracting the concentration of Fe^{2+} in the control group from that in the experimental group.

2.2.2. Removal of STZ

A 100 mL solution of 5 mg L^{-1} STZ was prepared and 0.3 g of the prepared catalyst was added. A 30 min adsorption experiment was conducted to investigate the adsorption capacity of the catalyst on STZ, after which a certain amount of H_2O_2 was added and the Fenton-like reaction was carried out for 60 min.

2.3. Analytical procedure

The physicochemical properties of the Tml were characterized to analyze the catalytic mechanism. Thermogravimetric analysis coupled with differential scanning calorimetry (TG-DSC) was used to determine the acceptable carbonization temperature of Tml crystal structure and it was performed by a NETZSCH STA 449F3. The surface morphology, crystal structure, surface area and elemental content of the catalysts were examined by scanning electron microscopy (SEM), transmission

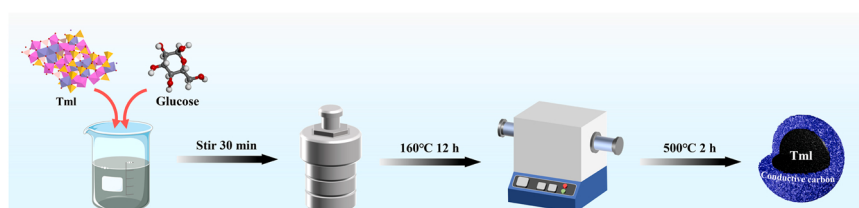


Fig. 1. Diagram of the Tml@C preparation process.

electron microscopy (TEM), X-ray diffraction (XRD), Brunner-Emmett-Teller (BET) and X-ray photoelectron spectroscopy (XPS), respectively. SEM was carried out by a Zeiss Merlin Compact. XRD was recorded with a SmartLab-SE. BET was tested by using an ASAP2460 surface area and porosimetry system. XPS was analyzed by a Thermo Scientific K-Alpha. Open circuit potential (OCP) and cyclic voltammetric curves (CV) were conducted using an electrochemical workstation model CHI-760E, where the CV sweep rate was set to 10 mV s^{-1} . The magnetic properties of catalysts were measured by a LakeShore 7404. Detection conditions for STZ and its intermediates are described in Text S2. The photoluminescence (PL) method was used to represent the generation of $\cdot\text{OH}$ [30]. Electron spin resonance (ESR) was performed by a Bruker EMXPLUS spectrometer. Fe^{2+} was determined by using 1,10-phenanthroline spectrophotometry method [20]. Total Fe was detected by a Perkin Optima 8300 ICP-OES.

2.4. Theoretical calculation

Theoretical calculations were carried out by using Dmol³ module of Materials Studio (Accelrys, SanDiego, CA) based on the density functional theory (DFT). The generalized gradient approximation (GGA) with the Perdew–Burke–Ernzerhof (PBE) exchange-correlation functional was utilized to treat all electronic energy of exchange correlation [31]. The core treated with All Electron. Basis set was employed by double numerical plus polarization (DNP). The k-points grid was set as $3 \times 3 \times 1$ and the k-points were generated thorough Monkhorst–Pack method [32]. The convergence criteria for the geometric optimization

was set as follows: (a) energy tolerance $2.0 \times 10^{-5} \text{ Ha}$, (b) maximum force tolerance $0.004 \text{ Ha/}\text{\AA}$, and (c) maximum displacement tolerance 0.005 \AA . The conductive carbon was modeled as a $4 \times 4 \times 1$ graphene supercell with vacuum layer of 15 \AA .

The geometry of the STZ was optimized by Gaussian16 A.03 using the M062x density function and the 6–311 +G(d,p) basis set [33,34]. The effect of water was considered using the solvation model of density (SMD) [35]. Electrostatic potential (ESP), average localized ionization energy (ALIE) and frontier molecular orbitals (HOMO and LUMO) were calculated with Multiwfn 3.8 and plotted by VMD 1.9 for the iso-planar [36,37].

3. Results and discussion

3.1. The piezoelectric properties of Tml in different sizes

The size of the particles affects the piezoelectric properties of Tml [38,39]. As shown in Fig. 2a, different sizes of Tml show different abilities to reduce Fe^{3+} to Fe^{2+} . When $300 \mu\text{M}$ Fe^{3+} was added to the system, the smallest size of Tml had the greatest ability to reduce Fe^{3+} at $25.51 \pm 0.57 \mu\text{M}$ (after deducting the dissolved amount of Tml itself shown in Fig. S1a). The reason Tml can promote the reduction of Fe^{3+} is the interfacial electric field generated when Tml is being stirred [40]. As shown in Fig. 2b, Tml had no Fe^{3+} reduction ability at a particle size of 2.5 mm , but the Fe^{3+} reduction efficiency increased with the decreasing Tml particle size, up to $8.50 \pm 0.19 \%$. Moreover, as shown in Fig. S1b, the reduction of Fe^{3+} followed a pseudo-first-order kinetic law for the

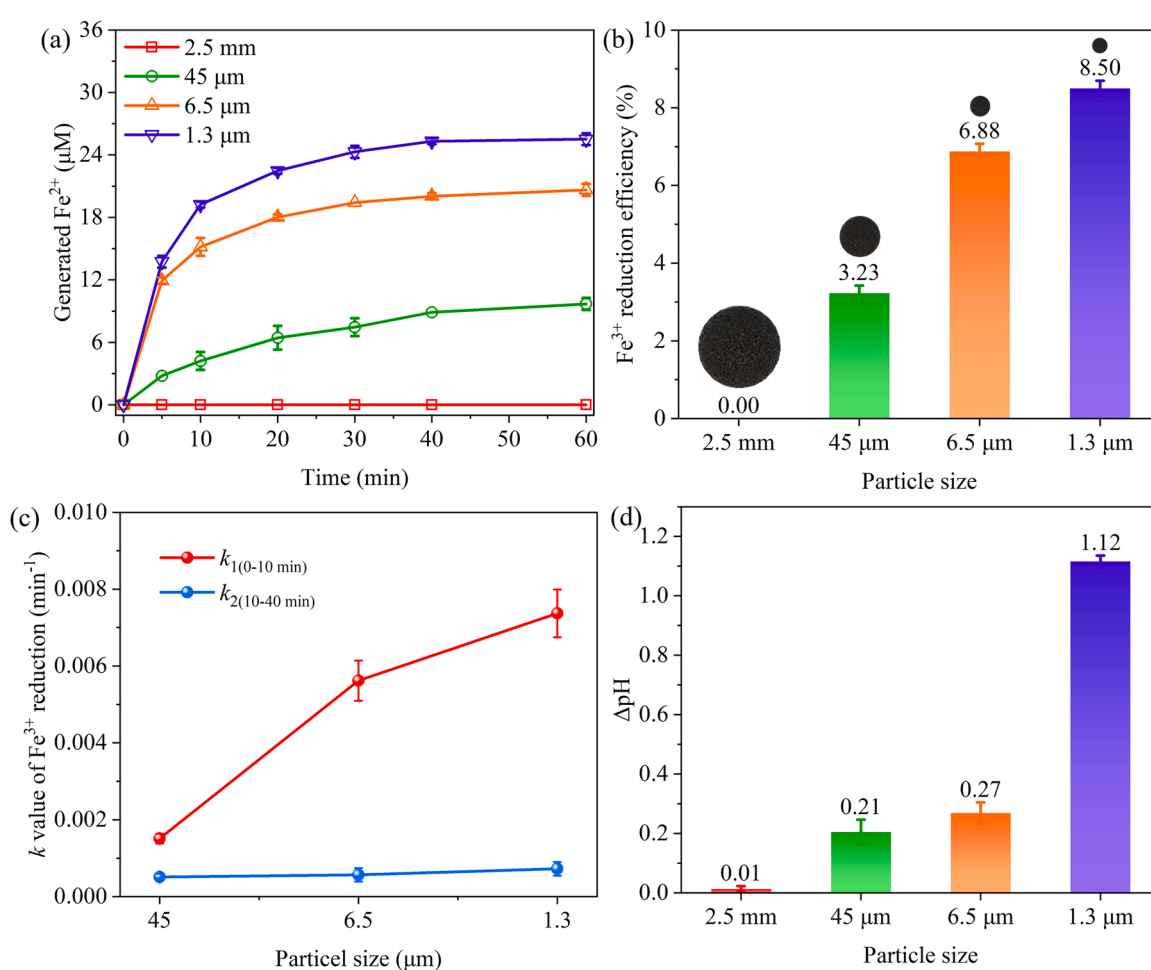
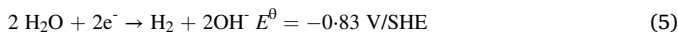


Fig. 2. The concentration of the (a) generated Fe^{2+} after adding $300 \mu\text{M}$ Fe^{3+} to water and (b) Fe^{3+} reduction efficiency with Tml of different sizes. (c) Plots of k value of Fe^{3+} reduction versus particle size. (d) pH changes with Tml of different sizes. Conditions: 0.3 g Tml , initial $\text{pH} = 3$ and N_2 protection rate = 400 mL min^{-1} .

first 40 min of the reaction with a fast reaction stage (k_1) and a slow reaction stage (k_2). Furthermore, according to Fig. 2c, the k value of Fe^{3+} reduction and Tml size decreasing are positively correlated. This is because piezoelectric materials such as Tml are subject to domain inversion, and their piezoelectric constant has the highest value in the size range of about 1 μm [41,42].

This interfacial electric field can be demonstrated by the change of pH in the system by Tml. As shown in Eq. (5) and Eq. (6), the interface electric field of Tml can electrolyze water and adsorb hydrogen ions to generate hydrogen [43]. As a result, as shown in Fig. 2d, this leads to a system with excess OH^- and thus a higher pH. Among them, the highest pH variation was observed for the Tml system with an average size of 1.3 μm , indicating that Tml of this size has the strongest interfacial electric field. However, the maximum reduction of Fe^{3+} was only 8.50% of the initial Fe^{3+} and was not effectively enough. Furthermore, the piezoelectric effect of Tml increased the pH value of the solution, which was not beneficial for the presence of iron in ionic form. Therefore, modification of pristine Tml was required to promote its ability to reduce Fe^{3+} to Fe^{2+} . The average size of the Tml used subsequently was 1.3 μm .



3.2. Characterization of Tml@Cx catalysts

The temperature that Tml can withstand was first determined by TG-DSC experiments before it was modified. As shown in Fig. 3a, there are two heat absorption peaks at 713.2 $^\circ\text{C}$ and 903.7 $^\circ\text{C}$, accompanied by a mass loss of 2.30% and 2.32%, respectively. This is because Tml undergoes a phase transition at high temperatures and releases OH groups in the crystal structure [44]. Based on the results of TG-DSC, a carbonization temperature of 500 $^\circ\text{C}$, which does not cause phase changes, was chosen to prepare Tml encapsulated with different carbon contents. As shown in Fig. S2, the corners of the Tml particles became more rounded and the surface became smoother after the carbon coating. The XRD

results in Fig. 3b indicate that the Tml before modification belongs to iron Tml, $\text{NaFe}_3\text{Al}_6(\text{BO}_3)_3\text{Si}_6\text{O}_{18}(\text{OH})_4$ (PDF#43-1464) [24]. The peak at 20 of 26.5 $^\circ$ in the XRD diffraction pattern was significantly enhanced when the Tml was coated with carbon. Compare with the PDF standard cards, the peak corresponds to the (0 0 2) diffraction peak of graphite [45]. The results show the successful preparation of Tml@C. In addition, as the amount of conductive carbon modification increases, its specific surface area and total pore volume also rise, which assists to improve the contact probability of the catalyst interface with Fe^{3+} in solution (Fig. 3c).

Further TEM experiments were carried out to verify the XRD results. As shown in Fig. 3d, the Tml@C2 TEM diagram shows that the modified Tml has a core-shell structure with Tml as the core and graphite as the shell. The fingerprint analysis in Fig. 3e shows that there is not only (1 0 1) crystal faces of iron Tml in Tml@C2, but also (0 0 2) crystal faces of graphite. In addition, as shown in Fig. 3f, as the amount of carbon modification increases, the peak at the binding energy of 284.4 eV gradually strengthens, which corresponds to the binding energy of C1s. The XPS results once again validate the successful preparation of a carbon coated Tml catalyst, which is consistent with the XRD and TEM results.

3.3. Promotion of Fe^{2+} regeneration by Tml@Cx catalysts

Fig. 4a represents the ability of Tml modified with different amount of conductive carbon to reduce Fe^{3+} . Cladding carbon can promote Fe^{3+} reduction, but excessive carbon modification was instead detrimental to Fe^{3+} reduction. As shown in Fig. 4a, Tml@C2 reduced Fe^{3+} most strongly, reducing $261.04 \pm 1.43 \mu\text{M}$ when 300 μM Fe^{3+} was added (after deducting the dissolved amount of Tml itself shown in Fig. S3). As shown in Fig. 4b, the Fe^{3+} reduction rate was as high as $87.01 \pm 0.48 \%$, which was 10.24 times that before modification. This is because the electric field formed at the Tml interface reduces the energy barrier for electrons activated by the conductive carbon, significantly enhancing the reduction of Fe^{3+} to Fe^{2+} [46]. However, the reduction efficiency of Fe^{3+} decreased when the Tml was overcoating with conductive carbon because the weakening of the electric field could limit the electron-donating ability of conductive carbon. Moreover, the electron

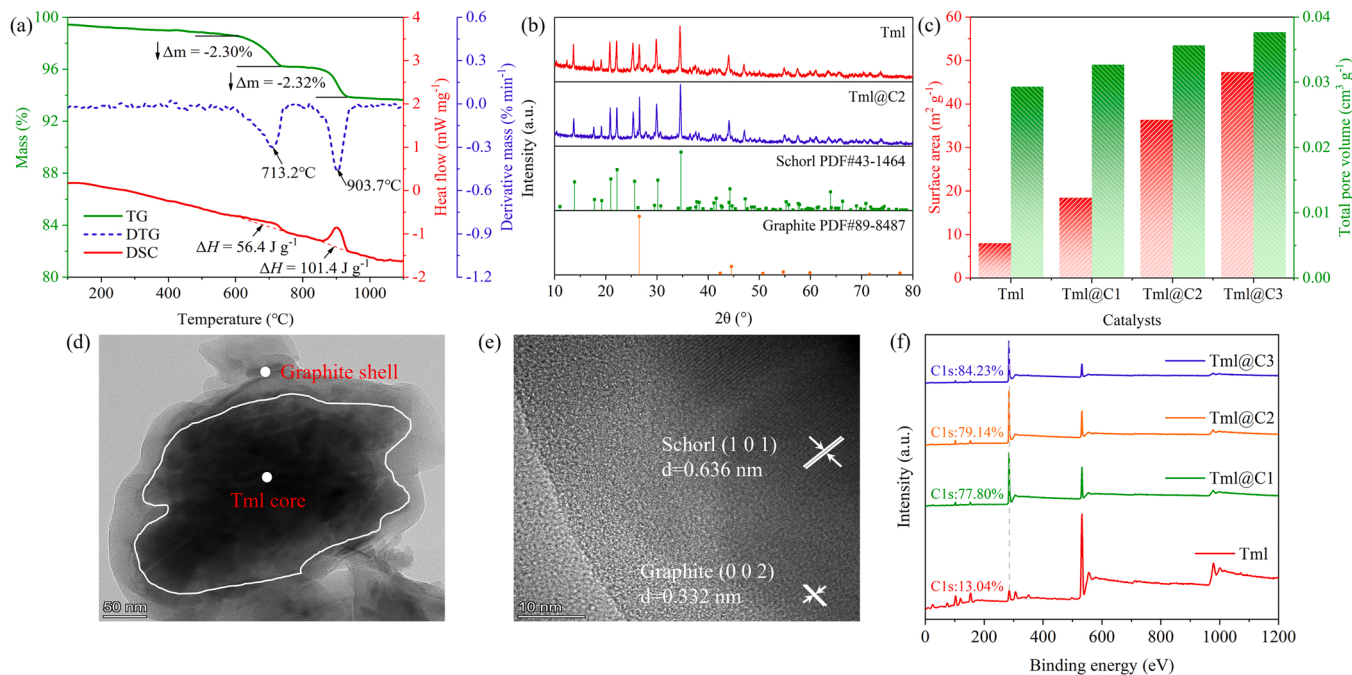


Fig. 3. (a) TG-DSC curves of Tml. (b) XRD patterns of Tml and Tml@C2. (c) Surface area and average pore diameter of different Tml. (d) TEM and (e) HR-TEM image of Tml@C2. (f) XPS spectrum of different Tml.

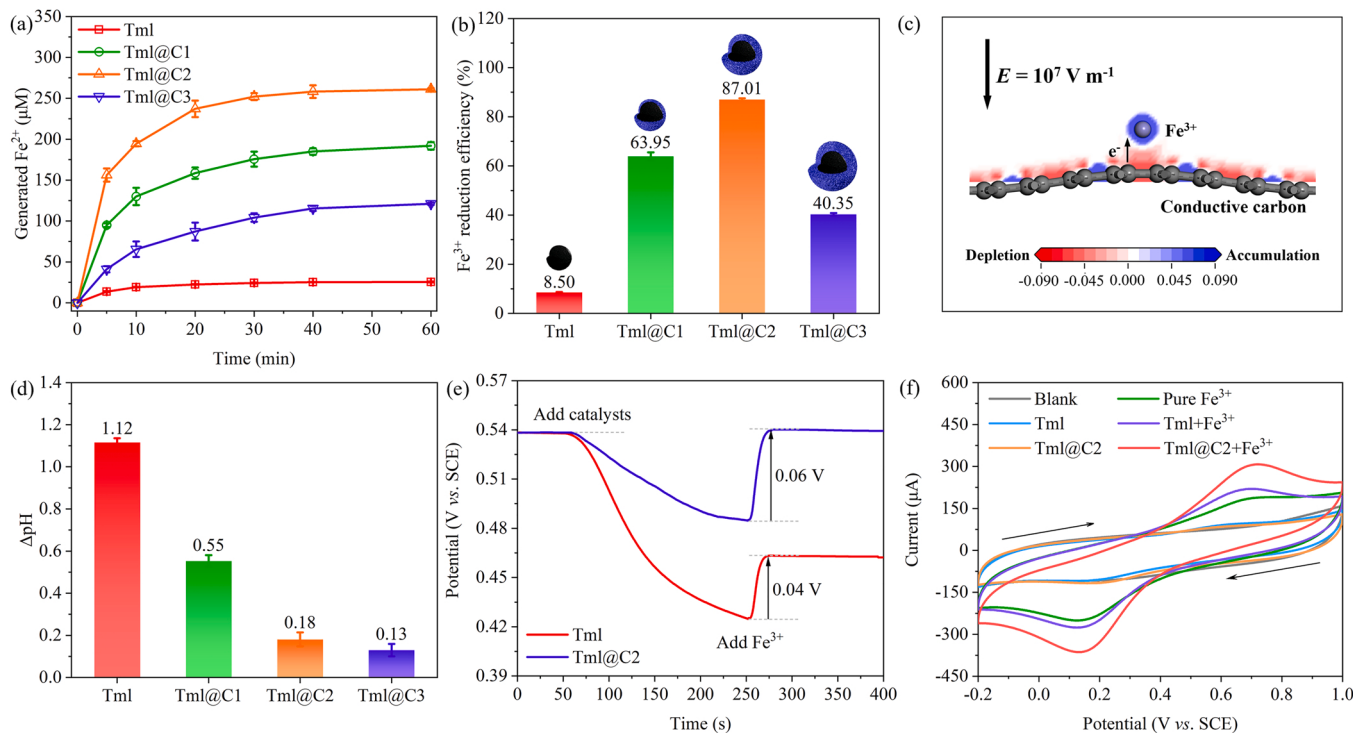


Fig. 4. The concentration of the (a) generated Fe^{2+} after adding 300 μM Fe^{3+} to water and (b) Fe^{3+} reduction efficiency with different catalysts. (c) Deformation charge density of Fe^{3+} -conductive carbon in the presence of the electric field. (d) pH changes with different catalysts. (e) OCP and (f) CV curves of different systems. Conditions: 0.3 g catalysts, initial pH = 3, 300 μM Fe^{3+} and N_2 protection rate = 400 mL min^{-1} .

transfer behavior was simulated by calculating deformation charge density [47]. As shown in Fig. 4c, in the presence of an electric field provided by Tml (a value of 10^7 V m^{-1} reported in the literature [40]), electrons are transferred from the conductive carbon to Fe^{3+} , facilitating its reduction to Fe^{2+} . Furthermore, Fig. 4d indicates that the increase in pH was less as the amount of carbon cladding increased, suggesting that more carbon cladding reduce the production of iron hydroxide. In addition, it can be seen from Fig. S3 that the coating of carbon effectively reduced the amount of Fe^{2+} dissolved. The amount of Tml dissolved before modification was $43.16 \pm 0.29 \mu\text{M}$, while the amount dissolved after modification was 77.44 %, 51.59 % and 51.59 % of that before modification, respectively. This is beneficial to maintain the catalytic activity of Tml.

To analyze the activity of the reduced Fe^{3+} at the Tml interface, OCP tests were carried out. As shown in Fig. 4e, the Tml potential decreased rapidly after addition, which was due to the electric field of Tml affecting the OCP. The subsequent addition of Fe^{3+} revealed that the Tml@C2 catalyst (0.06 V) showed a higher value of change in response potential to Fe^{3+} addition compared to Tml (0.04 V), indicating that the Tml@C2 catalyst improved the oxidation properties of Fe^{3+} [48]. Also, as shown in Fig. 4f, no redox peaks for Fe were seen in the different systems without the addition of Fe^{3+} . In the presence of Fe^{3+} , the addition of Tml increased the current response value, and the carbon modified Tml further increased the current response value, indicating that the amount of electrons gained and lost in the system was significantly enhanced, i.e. the redox reaction of Fe was strengthened [49]. The OCP and CV results indicate that the reactivity of Fe^{3+} became stronger in the Tml@C2 system, explaining the increased Fe^{3+} reduction efficiency in Fig. 4b compared to Tml.

3.4. Degradation of STZ by Fenton-like process

To make the modified Tml catalyst reusable while ensuring its high H_2O_2 catalytic activity in a wide pH range, Tml@C2@ Fe_3O_4 was prepared by loading Fe_3O_4 on the surface of Tml@C2. As can be seen from

Fig. S4, Tml@C2@ Fe_3O_4 can be separated by magnets, which facilitates reuse. It can be seen from Fig. 5a that the diffraction peaks of the Tml@C2@ Fe_3O_4 catalyst correspond to schrol (PDF#43–1464), graphite (PDF#89–8487) and Fe_3O_4 (PDF#89–0951), which has an additional crystal structure of Fe_3O_4 compared to the Tml@C2 catalyst in Fig. 3b, indicating that the properties of the internal structure are maintained after modification of Fe_3O_4 .

To highlight the piezoelectric effect of Tml@C2 on Fe_3O_4 , adsorption and Fenton-like catalysis tests were carried out using Fe_3O_4 and Tml@C2@ Fe_3O_4 as catalysts. The adsorption test was first carried out for 30 min to stabilize the adsorption, and then a Fenton-like reaction was conducted by adding different concentrations of H_2O_2 . As can be seen from Fig. 5b, the total removal efficiency was reached approximately 20 % by using Fe_3O_4 as a catalyst, significantly lower than that of Tml@C2@ Fe_3O_4 as a catalyst ($72.82 \pm 0.21 \%$). Moreover, Fig. 5c shows the PL intensity of TAOH at 60 min of reaction after the addition of 5 mM H_2O_2 with different catalyst systems. TAOH is a fluorescent substance formed by the reaction of TA with $\cdot\text{OH}$ and its fluorescence intensity is an indirect indication of the amount of $\cdot\text{OH}$ in the system [50]. As shown in Fig. 5c, the higher fluorescence value was obtained for Tml@C2@ Fe_3O_4 than Fe_3O_4 , indicating that the more concentration of $\cdot\text{OH}$ was produced in this system when catalyzed by the piezoelectric effect.

As shown in Fig. 5d, the pollutant removal rate reached approximately 33 % after 30 min of adsorption. Afterwards, when 1 mM, 2 mM and 5 mM H_2O_2 was added for 60 min, the removal of STZ reached $58.77 \pm 0.56 \%$, $65.49 \pm 2.28 \%$ and $72.82 \pm 0.21 \%$, respectively. Therefore, 5 mM was chosen as the H_2O_2 dosing amount for the subsequent Fenton experiments. In Fig. 5e, it was found that when the pH was 3 and 5, more than 99 % of STZ could be removed within 10 min after adding H_2O_2 , and 100 % of STZ could be removed after 30 min and 50 min of reaction. However, when the pH was increased to 7 and 9, the removal rates were $72.82 \pm 0.21 \%$ and $53.66 \pm 2.78 \%$, respectively. The results indicated that the performance of the catalyst was heavily influenced by the pH value due to the following two reasons: (1) as

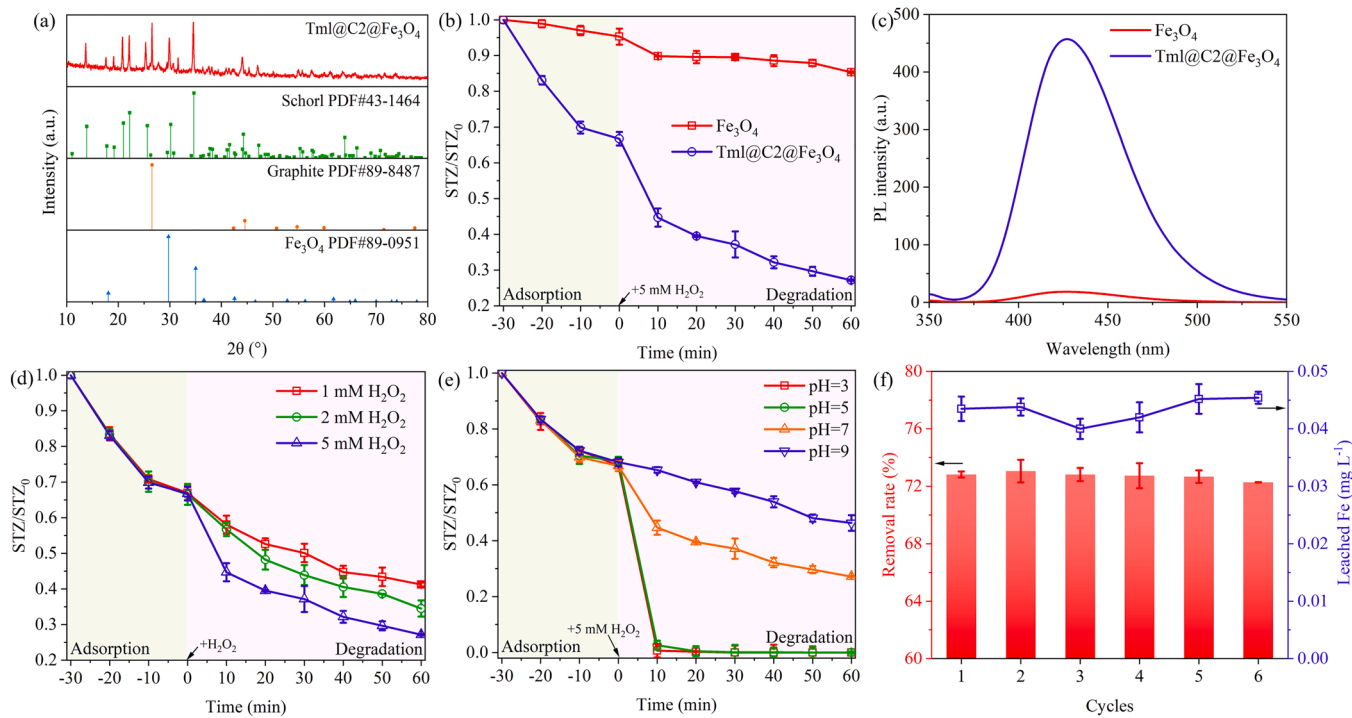


Fig. 5. (a) XRD spectra of Tml@C2 @Fe₃O₄. (b) STZ removal and (c) PL intensity of TAOH using Fe₃O₄ and Tml@C2 @Fe₃O₄ catalysts. STZ removal with different (d) dosages of H₂O₂ and (e) pH. (f) Durability of Tml@C2 @Fe₃O₄ catalyst. Conditions: 0.3 g Tml@C2 @Fe₃O₄, 5 mM H₂O₂, 5 mg L⁻¹ STZ and neutral pH.

shown in Fig. S5, more amount of iron was dissolved under acidic conditions, which facilitated a more rapid homogeneous reaction than the heterogeneous reaction [51]; (2) according to the Nernst equation, Eq. (7) can be derived to calculate the redox potential of ·OH under different pH conditions [52]. Obviously, the redox potential of ·OH gradually decreases with pH increase, and the ability to attack the STZ structure will be weakened.

$$E = E^0 - 0.059pH \quad (7)$$

In addition, the prepared catalysts were compared with other Fenton-like catalysts in STZ removal efficiency (details were listed in Table S1), demonstrating that the prepared catalysts have good STZ removal ability even at neutral pH.

To reduce the cost of Fenton-like systems, catalysts need to have

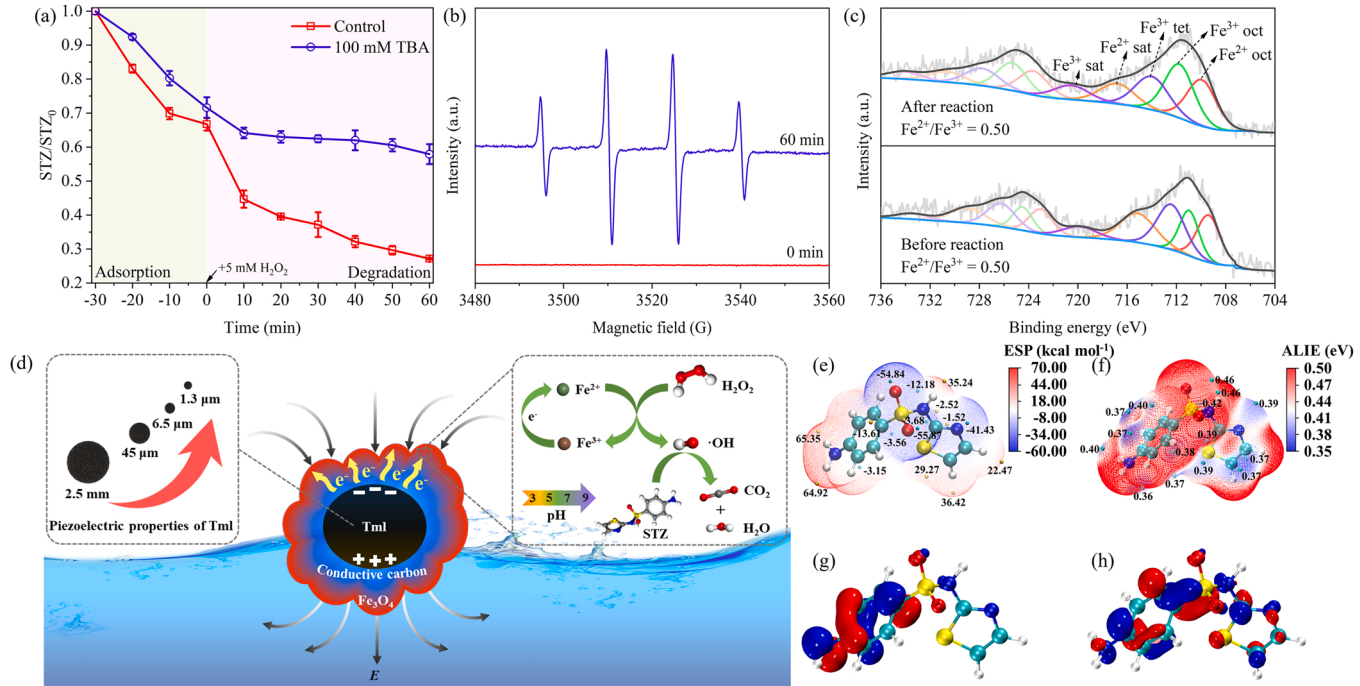


Fig. 6. (a) Effect of 100 mM TBA on STZ removal. (b) ESR spectra of DMPO-OH adducts. (c) Fe 2p XPS spectra of Tml@C2 @Fe₃O₄ before and after reaction. Conditions: 0.3 g Tml@C2 @Fe₃O₄, 5 mM H₂O₂, 5 mg L⁻¹ STZ and neutral pH. (d) Scheme of Fenton-like system. (e) ESP, (f) ALIE, (g) HOMO and (h) LUMO of STZ.

good durability properties. As shown in Fig. 5f, the removal of STZ by Tml@C2 @Fe₃O₄ was still able to reach more than 72 % after 6 times of reuse, indicating that the catalyst can be reused. Furthermore, the amount of dissolved Fe corresponding to the durability of the catalyst remains at a low level of less than 0.05 mg L⁻¹. In addition, a comparison of the surface morphology of Tml@C2@Fe₃O₄ before and after the reaction showed no significant change in particle size and roughness (Fig. S6). Further, the crystal structure was analyzed by XRD spectroscopy before and after the reaction (Fig. S7). The catalyst still had diffraction peaks of Tml (PDF#43–1464), graphite (PDF#89–8487) and Fe₃O₄ (PDF#89–0951) after the reaction, again verifying the stability of the catalyst.

3.5. Mechanism of Fenton-like process

The active substances in the system that play a key role in the degradation of pollutants were examined by the addition of capture agents. The reaction rate constant of TBA for ·OH is as high as $(3.8\text{--}7.6) \times 10^8 \text{ min}^{-1}$ and has a lower dielectric constant than ethanol, making it more accessible to the catalyst surface and thus trapping ·OH at the catalyst interface and in solution simultaneously [53,54]. As can be seen in Fig. 6a, the adsorption and removal of STZ by the Tml@C2 @Fe₃O₄ catalyst decreased by nearly 5 % after the addition of 100 mM TBA, due to the excess TBA occupying the adsorption sites of the catalyst. When the reaction was carried out for 60 min after the addition of 5 mM H₂O₂, the group without TBA could remove 39.57 \pm 1.69 % of the STZ, while the group with TBA could only remove 13.67 \pm 0.12 % of the STZ. The inhibition of STZ removal by 100 mM TBA was calculated to be over 65 %, indicating that it is the ·OH that plays the main active role in this system. Further, the presence of ·OH in the system was verified by ESR experiments. As can be seen in Fig. 6b, no peaks were present in the absence of the Fenton-like reaction, while after 60 min of reaction, the typical characteristic peak of DMPO-·OH with a peak intensity ratio of 1:2:2:1 appeared, demonstrating the formation of ·OH in the system [55].

Fig. 4a shows that the conductive carbon modified Tml@C2 can efficiently reduce Fe³⁺ in solution at acidic conditions, but the STZ removal experiments were performed under neutral conditions using Tml@C2@Fe₃O₄ as a catalyst. Fig. S5 shows that the amount of dissolved Fe from Tml@C2@Fe₃O₄ was small, indicating that the interfacial Fenton reaction dominated. Therefore, the effect of the piezoelectric electric field of Tml on Fe₃O₄ needs to be examined. As shown in Fig. 6c, the outermost Fe₃O₄ layer of the core-shell structure of the catalyst had a Fe²⁺/Fe³⁺ ratio of 0.50 before the reaction, while its value remained at 0.50 after the reaction, indicating that the piezoelectric field could efficiently reduce not only Fe³⁺ in solution but also Fe³⁺ at the interface.

Based on the results of this study, a mechanism for the degradation of STZ by the system when Tml@C2@Fe₃O₄ was used as a catalyst for the Fenton-like system was proposed. As can be seen from Fig. 6d, the mechanism of the Fenton-like reaction system is as follows: (I) as the Tml boundary is subjected to changing forces in the system under stirring conditions, a piezoelectric field is subsequently generated on the surface; (II) the smaller the size of Tml has a stronger piezoelectric effect, promoting the reduction of Fe³⁺ to Fe²⁺; (III) the conductive carbon modified on the surface of Tml is affected by the piezoelectric field, releasing the free electrons within the conductive carbon; (IV) the free electrons encounter Fe³⁺ at the catalyst interface or in solution and reduce it to Fe²⁺, promoting the regeneration of Fe²⁺ in the Fenton-like system; (V) at the same time, H₂O₂ is catalyzed by the catalyst to carry out a Fenton-like reaction to generate a strong oxidizing radical ·OH; VI) eventually ·OH attacks STZ, destroying its molecular structure and generating degradation products.

Based on density functional theory, theoretical calculations lead to the possible locations for ·OH attack on the molecular structure. The more negative the electrostatic potential, the more likely it is to attract an electrophilic reagent to react, and it is generally accepted that the

atom closest to the location of the electrostatic minimum on the surface of the molecule will be the most likely site for an electrophilic reaction [56]. As shown in Fig. 6e, the sulfonamide group and the thiazole ring in the STZ structure readily attract electrophilic reagents. In addition, after completing the first step of the first guess, the specific attack location of ·OH needs to be combined with ALIE analysis, because ESP and ALIE are complementary, and the smaller the ALIE value, the higher the possibility for radical attack [57]. The high reactivity of the aniline and thiazole rings can be seen in Fig. 6f. Further, the frontier molecular orbitals theory shows that HOMO is the site vulnerable to attack by electrophilic reagents [58]. This led to the speculation of sites where the STZ molecular structure might react with the electrophilic reagent ·OH. As can be seen from the HOMO and LUMO distributions in Figs. 6g and 6h, aniline is mainly attacked by electrophilic reagents, while the thiazole ring has low activity.

Combining the above theoretical calculations and the results of the liquid-phase mass spectrometry coupled detection (Table S2), a possible pathway for the degradation of STZ is proposed, as shown in Fig. S8. The degradation pathways of STZ can be divided into three main pathways: (I) the sulfonamide group in STZ is attacked by ·OH, resulting in the breaking of the S-N bond to produce P1-C₃H₄N₂S and P2-C₆H₇NO₃S, followed by further hydroxylation of P2 to produce P3-C₆H₇NO and P4-C₆H₇NO₂; (II) the amino group in the aniline structure of STZ is attacked by ·OH to produce P5-C₉H₇N₃O₄S₂, followed by hydroxylation to produce P6-C₉H₈N₂O₃S₂ and P7-C₉H₈N₂O₄S₂; (III) direct hydroxylation of the aniline structure of STZ with ·OH to produce P8-C₉H₉N₃O₄S₂.

4. Conclusions

In conclusion, catalysts that promote Fe³⁺/Fe²⁺ cycle were prepared by surface modification of Tml with conductive carbon and Fe₃O₄, enabling the Fenton-like system to efficiently remove STZ over a wide pH range. The smaller the particle size of Tml, the stronger its piezoelectric effect. Conductive carbon transfers electrons to Fe³⁺ on the Tml surface in the presence of an electric field due to the deformation of charge density. Compared to Tml without modified conductive carbon, the reduction efficiency of Fe³⁺ with modified conductive carbon increased to 87.01 %, 10.24 times of that of the former. Under neutral conditions, the adsorption of STZ by Tml@C2@Fe₃O₄ reached approximately 33% after 30 min. Later when 5 mM H₂O₂ was added the removal of STZ reached 72.82 % after 60 min. ·OH is the main radical in the system and the addition of the trapping agent inhibited the removal of STZ by more than 65 %. Combining theoretical calculations and experimental results, aniline and sulfonamide groups were most easily attacked by ·OH. In addition, the catalyst has good stability and can be reused up to six times.

CRediT authorship contribution statement

Yingshi Zhu: Conceptualization, Methodology, Software, Formal analysis, Investigation, Data curation, Writing – Original Draft, Visualization, **Jianqiu Zhu:** Supervision, Resources, Project administration, Writing – Review & Editing, **Huabin ShenTu:** Supervision, Project administration, Writing – Review & Editing, **Yanfei Wei:** Supervision, Project administration, Writing – Review & Editing **Jun Wei:** Supervision, Writing, – Review & Editing, **Lecheng Lei:** Supervision, Writing – Review & Editing, **Funding acquisition, Yuru Li:** Supervision, Writing – Review & Editing, **Tao Yu:** Supervision, Writing – Review & Editing, **Zhongjian Li:** Supervision, Writing – Review & Editing, **Yang Hou:** Supervision, Writing – Review & Editing, **Bin Yang:** Validation, Supervision, Resources, Project administration, Writing – Review & Editing, **Funding acquisition.**

Declaration of Competing Interest

The authors declare that they have no known competing financial

interests or personal relationships that could have appeared to influence the work reported in this paper.

Data availability

Data will be made available on request.

Acknowledgments

This work was financially supported by the “Lingyan” R&D Plan Project of Zhejiang Province (2023C03140) and the National Natural Science Foundation of China (22278366, 22238008 and 21878271).

Appendix A. Supporting information

Supplementary data associated with this article can be found in the online version at [doi:10.1016/j.apcatb.2023.122824](https://doi.org/10.1016/j.apcatb.2023.122824).

References

- Q. Yang, Y. Gao, J. Ke, P.L. Show, Y. Ge, Y. Liu, R. Guo, J. Chen, Antibiotics: an overview on the environmental occurrence, toxicity, degradation, and removal methods, *Bioengineered* 12 (2021) 7376–7416, <https://doi.org/10.1080/21655979.2021.1974657>.
- J. Lyu, L. Yang, L. Zhang, B. Ye, L. Wang, Antibiotics in soil and water in China – a systematic review and source analysis, *Environ. Pollut.* 266 (2020), 115147, <https://doi.org/10.1016/j.envpol.2020.115147>.
- W. Duan, H. Cui, X. Jia, X. Huang, Occurrence and ecotoxicity of sulfonamides in the aquatic environment: a review, *Sci. Total Environ.* 820 (2022), 153178, <https://doi.org/10.1016/j.scitotenv.2022.153178>.
- M. Geng, Y. Tang, K. Liu, K. Huang, S. Yan, P. Ding, J. Zhang, B. Wang, S. Wang, S. Li, X. Wu, Y. Cao, F. Tao, Prenatal low-dose antibiotic exposure and children allergic diseases at 4 years of age: a prospective birth cohort study, *Ecotoxicol. Environ. Saf.* 225 (2021), 112736, <https://doi.org/10.1016/j.ecoenv.2021.112736>.
- J. Feng, Q. Tao, H. Lan, Y. Xia, Q. Dai, Electrochemical oxidation of sulfamethoxazole by nitrogen-doped carbon nanosheets composite PbO₂ electrode: kinetics and mechanism, *Chemosphere* 286 (2022), 131610, <https://doi.org/10.1016/j.chemosphere.2021.131610>.
- M.Z. Akbari, Y. Xu, Z. Lu, L. Peng, Review of antibiotics treatment by advance oxidation processes, *Environ. Adv.* 5 (2021), 100111, <https://doi.org/10.1016/j.envadv.2021.100111>.
- J. Wang, R. Zhuan, Degradation of antibiotics by advanced oxidation processes: an overview, *Sci. Total Environ.* 701 (2020), 135023, <https://doi.org/10.1016/j.scitotenv.2019.135023>.
- A.S. Oberoi, Y. Jia, H. Zhang, S.K. Khanal, H. Lu, Insights into the fate and removal of antibiotics in engineered biological treatment systems: a critical review, *Environ. Sci. Technol.* 53 (2019) 7234–7264, <https://doi.org/10.1021/acs.est.9b01131>.
- N. Thomas, D.D. Dionysiou, S.C. Pillai, Heterogeneous Fenton catalysts: a review of recent advances, *J. Hazard. Mater.* 404 (2021), 124082, <https://doi.org/10.1016/j.jhazmat.2020.124082>.
- J.P. Ribeiro, M.I. Nunes, Recent trends and developments in Fenton processes for industrial wastewater treatment – a critical review, *Environ. Res.* 197 (2021), 110957, <https://doi.org/10.1016/j.enres.2021.110957>.
- X. Nie, G. Li, S. Li, Y. Luo, W. Luo, Q. Wan, T. An, Highly efficient adsorption and catalytic degradation of ciprofloxacin by a novel heterogeneous Fenton catalyst of hexapod-like pyrite nanosheets mineral clusters, *Appl. Catal. B-Environ.* 300 (2022), 120734, <https://doi.org/10.1016/j.apcatb.2021.120734>.
- H. Zhou, H. Zhang, Y. He, B. Huang, C. Zhou, G. Yao, B. Lai, Critical review of reductant-enhanced peroxide activation processes: trade-off between accelerated Fe³⁺/Fe²⁺ cycle and quenching reactions, *Appl. Catal. B-Environ.* 286 (2021), 119900, <https://doi.org/10.1016/j.apcatb.2021.119900>.
- L. Fan, J. Xie, Z. Zhang, Y. Zheng, D. Yao, T. Li, Magnetically recoverable Fe₃O₄@polydopamine nanocomposite as an excellent co-catalyst for Fe³⁺ reduction in advanced oxidation processes, *J. Environ. Sci.* 92 (2020) 69–78, <https://doi.org/10.1016/j.jes.2020.02.006>.
- M.D.N. Ramos, G.L.S. Silva, T.L. Lessa, A. Aguiar, Study of kinetic parameters related to dyes oxidation in ascorbic acid-mediated Fenton processes, *Process Saf. Environ.* 168 (2022) 1131–1141, <https://doi.org/10.1016/j.psep.2022.10.083>.
- T. Pan, Y. Wang, X. Yang, X. Huang, R. Qiu, Gallic acid accelerated BDE47 degradation in PMS/Fe(II) system: oxidation intermediates autocatalyzed redox cycling of iron, *Chem. Eng. J.* 384 (2020), 123248, <https://doi.org/10.1016/j.cej.2019.123248>.
- U. Farooq, F. Wang, J. Shang, M. Zeeshan Shahid, W. Akram, X. Wang, Heightening effects of cysteine on degradation of trichloroethylene in Fe³⁺/SPC process, *Chem. Eng. J.* 454 (2023), 139996, <https://doi.org/10.1016/j.cej.2022.139996>.
- N.A. Zubir, C. Yacou, J. Motuzas, X. Zhang, X.S. Zhao, J.C. Diniz Da Costa, The sacrificial role of graphene oxide in stabilising a Fenton-like catalyst GO-Fe₃O₄, *Chem. Commun.* 51 (2015) 9291–9293, <https://doi.org/10.1039/C5CC02292D>.
- J. Zhu, J. Ma, L. Liu, S. Zhang, L. Zhao, H. Jin, K. Zhang, Carbon supported “core-shell structure” of Fe nanoparticles for enhanced Fenton reaction activity and magnetic separation, *Environ. Sci. Pollut. R.* 30 (2023) 7207–7217, <https://doi.org/10.1007/s11356-022-22754-x>.
- Z. Cao, X. Wen, P. Chen, F. Yang, X. Ou, S. Wang, H. Zhong, Synthesis of a novel heterogeneous Fenton catalyst and promote the degradation of methylene blue by fast regeneration of Fe²⁺, *Colloid Surf. A* 549 (2018) 94–104, <https://doi.org/10.1016/j.colsurfa.2018.04.009>.
- Y. Tang, J. Dou, Z. Lu, J. Xu, Y. He, Accelerating Fe²⁺/Fe³⁺ cycle via biochar to improve catalytic degradation efficiency of the Fe³⁺/Persulfate oxidation, *Environ. Pollut.* (2022), 120669, <https://doi.org/10.1016/j.envpol.2022.120669>.
- Y. Chu, H. Su, R. Lv, X. Zhang, Enhanced electro-reduction of Fe³⁺ to Fe²⁺ by acidified carbon nanotube-modified graphite cathode and its application in a novel Fenton process for p-nitrophenol degradation, *J. Water Process Eng.* 40 (2021), 101912, <https://doi.org/10.1016/j.jwpe.2020.101912>.
- L. Xu, L. Meng, X. Zhang, X. Mei, X. Guo, W. Li, P. Wang, L. Gan, Promoting Fe³⁺/Fe²⁺ cycling under visible light by synergistic interactions between P25 and small amount of Fenton reagents, *J. Hazard. Mater.* 379 (2019), 120795, <https://doi.org/10.1016/j.jhazmat.2019.120795>.
- P. Zhao, Y. Jiang, Z. Tang, Y. Li, B. Sun, Y. Wu, J. Wu, Y. Liu, W. Bu, Constructing electron levers in perovskite nanocrystals to regulate the local electron density for intensive chemodynamic therapy, *Angew. Chem. Int. Ed.* 60 (2021) 8905–8912, <https://doi.org/10.1002/anie.202100864>.
- Y. Zhu, S. Qiu, W. Tang, F. Deng, F. Ma, Y. Zheng, H. Xie, Sustainable Fe³⁺ reduction by Fe₃O₄@tourmaline in Fenton-like system, *Chem. Eng. J.* 437 (2022), 135480, <https://doi.org/10.1016/j.cej.2022.135480>.
- R. Li, Q. Guo, Z. Shi, J. Pei, Effects of conductive carbon black on PZT/PVDF composites, *Ferroelectrics* 526 (2018) 176–186, <https://doi.org/10.1080/00150193.2018.1456308>.
- J. Wang, J. Tang, Fe-based Fenton-like catalysts for water treatment: preparation, characterization and modification, *Chemosphere* 276 (2021), 130177, <https://doi.org/10.1016/j.chemosphere.2021.130177>.
- T. Zhang, Y. Wen, Z. Pan, Y. Kuwahara, K. Mori, H. Yamashita, Y. Zhao, X. Qian, Overcoming acidic H₂O₂/Fe(II/III) redox-induced low H₂O₂ utilization efficiency by carbon quantum dots Fenton-like catalysis, *Environ. Sci. Technol.* 56 (2022) 2617–2625, <https://doi.org/10.1021/acs.est.1c06276>.
- W. Luo, L. Zhu, N. Wang, H. Tang, M. Cao, Y. She, Efficient removal of organic pollutants with magnetic nanoscaled BiFeO₃ as a reusable heterogeneous Fenton-like catalyst, *Environ. Sci. Technol.* 44 (2010) 1786–1791, <https://doi.org/10.1021/es903390g>.
- B. Jain, A.K. Singh, H. Kim, E. Lichtfouse, V.K. Sharma, Treatment of organic pollutants by homogeneous and heterogeneous Fenton reaction processes, *Environ. Chem. Lett.* 16 (2018) 947–967, <https://doi.org/10.1007/s10311-018-0738-3>.
- F. Deng, S. Li, M. Zhou, Y. Zhu, S. Qiu, K. Li, F. Ma, J. Jiang, A biochar modified nickel-foam cathode with iron-foam catalyst in electro-Fenton for sulfamerazine degradation, *Appl. Catal. B-Environ.* 256 (2019), 117796, <https://doi.org/10.1016/j.apcatb.2019.117796>.
- J.P. Perdew, K. Burke, M. Ernzerhof, Generalized gradient approximation made simple, *Phys. Rev. Lett.* 77 (1996) 3865–3868, <https://doi.org/10.1103/PhysRevLett.77.3865>.
- L. Hu, X. Hu, X. Wu, C. Du, Y. Dai, J. Deng, Density functional calculation of transition metal adatom adsorption on graphene, *Phys. B Condens. Matter* 405 (2010) 3337–3341, <https://doi.org/10.1016/j.physb.2010.05.001>.
- M.J. Frisch, G.W. Trucks, H.B. Schlegel, G.E. Scuseria, M.A. Robb, J.R. Cheeseman, G. Scalmani, V. Barone, G.A. Petersson, H. Nakatsuji, X. Li, M. Caricato, A.V. Marenich, J. Bloino, B.G. Janesko, R. Gomperts, B. Mennucci, H.P. Hratchian, J.V. Ortiz, A.F. Izmaylov, J.L. Sonnenberg, Williams, F. Ding, F. Lipparini, F. Egidi, J. Goings, B. Peng, A. Petrone, T. Henderson, D. Ranasinghe, V.G. Zakrzewski, J. Gao, N. Rega, G. Zheng, W. Liang, M. Hada, M. Ehara, K. Toyota, R. Fukuda, J. Hasegawa, M. Ishida, T. Nakajima, Y. Honda, O. Kitao, H. Nakai, T. Vreven, K. Throssell, J.A. Montgomery Jr., J.E. Peralta, F. Ogliaro, M.J. Bearpark, J.J. Heyd, E. N. Brothers, K.N. Kudin, V.N. Staroverov, T.A. Keith, R. Kobayashi, J. Normand, K. Raghavachari, A.P. Rendell, J.C. Burant, S.S. Iyengar, J. Tomasi, M. Cossi, J.M. Millam, M. Klene, C. Adamo, R. Cammi, J.W. Ochterski, R.L. Martin, K. Morokuma, O. Farkas, J.B. Foresman, D.J. Fox, Gaussian 16 Rev. A.03, Wallingford, CT, 2016.
- Y. Zheng, J. He, S. Qiu, D. Yu, Y. Zhu, H. Pang, J. Zhang, Boosting hydrogen peroxide accumulation by a novel air-breathing gas diffusion electrode in electro-Fenton system, *Appl. Catal. B-Environ.* 316 (2022), 121617, <https://doi.org/10.1016/j.apcatb.2022.121617>.
- A.V. Marenich, C.J. Cramer, D.G. Truhlar, Universal solvation model based on solute electron density and on a continuum model of the solvent defined by the bulk dielectric constant and atomic surface tensions, *J. Phys. Chem. B* 113 (2009) 6378–6396, <https://doi.org/10.1021/jp810292n>.
- T. Lu, F. Chen, Multiwfns a multifunctional wavefunction analyzer, *J. Comput. Chem.* 33 (2012) 580–592, <https://doi.org/10.1002/jcc.22885>.
- W. Humphrey, A. Dalke, K. Schulten, VMD: visual molecular dynamics, *J. Mol. Graph. Graph* 14 (33–38) (1996) 27–28, [https://doi.org/10.1016/0263-7855\(96\)00018-5](https://doi.org/10.1016/0263-7855(96)00018-5).
- J. Zhang, P. Ji, Y. Wu, X. Zhao, Y. Tan, C. Wang, Strong piezoelectricity exhibited by large-grained BaTiO₃ ceramics, *Appl. Phys. Lett.* 104 (2014), 222909, <https://doi.org/10.1063/1.4881597>.
- D. Luo, H. Liu, H. Hao, Y. Li, S. Ouyang, Influence of particle size on piezoelectricity of piezo-composites, in: J. Wuhan Univ. Technol. Mater. Sci., 22, 2007, pp. 165–167, <https://doi.org/10.1007/s11595-005-1165-4>.
- T. Nakamura, T. Kubo, Tourmaline group crystals reaction with water, *Ferroelectrics* 137 (1992) 13–31, <https://doi.org/10.1080/00150199208015933>.

[41] Y. Huan, X. Wang, J. Fang, L. Li, I.W. Chen, Grain size effects on piezoelectric properties and domain structure of BaTiO₃ ceramics prepared by two-step sintering, *J. Am. Ceram. Soc.* 96 (2013) 3369–3371, <https://doi.org/10.1111/jace.12601>.

[42] T. Hoshina, Size effect of barium titanate: fine particles and ceramics, *J. Ceram. Soc. Jpn* 121 (2013) 156–161, <https://doi.org/10.2109/jcersj2.121.156>.

[43] Y. Nishi, A. Yazawa, K. Oguri, F. Kanazaki, T. Kaneko, pH self-controlling induced by tourmaline, *J. Intel. Mater. Syst. Struct.* 7 (1996) 260–263, <https://doi.org/10.1177/1045389x9600700303>.

[44] F. Wang, J. Meng, J. Liang, B. Fang, H. Zhang, Insight into the thermal behavior of tourmaline mineral, *JOM* 71 (2019) 2468–2474, <https://doi.org/10.1007/s11837-019-03391-1>.

[45] K.K. Jena, A. AlFantazi, A.T. Mayyas, Efficient and cost-effective hybrid composite materials based on thermoplastic polymer and recycled graphite, *Chem. Eng. J.* 430 (2022), 132667, <https://doi.org/10.1016/j.cej.2021.132667>.

[46] Z. Wu, H. Wang, K. Zheng, M. Xue, P. Cui, X. Tian, Incorporating strong polarity minerals of tourmaline with carbon nanotubes to improve the electrical and electromagnetic interference shielding properties, *J. Phys. Chem. C* 116 (2012) 12814–12818, <https://doi.org/10.1021/jp2121164>.

[47] S. Hu, X. Chen, Q. Li, F. Li, Z. Fan, H. Wang, B. Zheng, G. Wu, Fe³⁺ doping promoted N₂ photoxidation ability of honeycombed graphitic carbon nitride: the experimental and density functional theory simulation analysis, *Appl. Catal. B-Environ.* 201 (2017) 58–69, <https://doi.org/10.1016/j.apcatb.2016.08.002>.

[48] C. Zhou, P. Zhou, M. Sun, Y. Liu, H. Zhang, Z. Xiong, J. Liang, X. Duan, B. Lai, Nitrogen-doped carbon nanotubes enhanced Fenton chemistry: role of near-free iron(III) for sustainable iron(III)/iron(II) cycles, *Water Res.* 210 (2022), 117984, <https://doi.org/10.1016/j.watres.2021.117984>.

[49] Y.S. Choudhary, L. Jothi, G. Nageswaran, in: S. Thomas, R. Thomas, A. K. Zachariah, R.K. Mishra (Eds.), *Spectroscopic Methods for Nanomaterials Characterization*, Elsevier, 2017, pp. 19–54.

[50] F. Deng, J. Xie, O. Garcia-Rodriguez, B. Jing, Y. Zhu, Z. Chen, J. Hsu, J. Jiang, S. Bai, S. Qiu, A dynamic anode boosting sulfamerazine mineralization via electrochemical oxidation, *J. Mater. Chem. A* 10 (2021) 192–208, <https://doi.org/10.1039/DITA08095D>.

[51] W.P. Kwan, B.M. Voelker, Decomposition of hydrogen peroxide and organic compounds in the presence of dissolved iron and ferrihydrite, *Environ. Sci. Technol.* 36 (2002) 1467–1476, <https://doi.org/10.1021/es011109p>.

[52] Y. Li, W. Zhang, J. Niu, Y. Chen, Mechanism of photogenerated reactive oxygen species and correlation with the antibacterial properties of engineered metal-oxide nanoparticles, *ACS Nano* 6 (2012) 5164–5173, <https://doi.org/10.1021/nn300934k>.

[53] L. Wang, X. Lan, W. Peng, Z. Wang, Uncertainty and misinterpretation over identification, quantification and transformation of reactive species generated in catalytic oxidation processes: a review, *J. Hazard. Mater.* 408 (2021), 124436, <https://doi.org/10.1016/j.jhazmat.2020.124436>.

[54] J. Jing, X. Wang, M. Zhou, Electro-enhanced activation of peroxyxonosulfate by a novel perovskite-Ti₄O₇ composite anode with ultra-high efficiency and low energy consumption: the generation and dominant role of singlet oxygen, *Water Res.* 232 (2023), 119682, <https://doi.org/10.1016/j.watres.2023.119682>.

[55] F. Zhang, X. Li, Q. Zhao, G. Chen, Q. Zhang, High-performance In₂O₃@PANI core@shell architectures with ultralong charge carriers lifetime for photocatalytic degradation of gaseous 1,2-dichlorobenzene, *Appl. Catal. B-Environ.* 263 (2020), 118278, <https://doi.org/10.1016/j.apcatb.2019.118278>.

[56] M. Alcamí, O. Mó, M. Yáñez, in: J.S. Murray, K. Sen (Eds.), *Theoretical and Computational Chemistry*, Elsevier, 1996, pp. 407–456.

[57] K. Shiva Prasad, R.R. Pillai, S. Armaković, S.J. Armaković, Theoretical investigation on the reactivity and photophysical properties of cobalt(II) and manganese(II) complexes constructed using Schiff base ligands based on ALIE and TDDFT calculations, *Polyhedron* 129 (2017) 141–148, <https://doi.org/10.1016/j.poly.2017.03.049>.

[58] H. Wang, W. Guo, R. Yin, J. Du, Q. Wu, H. Luo, B. Liu, F. Sseguya, N. Ren, Biochar-induced Fe(III) reduction for persulfate activation in sulfamethoxazole degradation: Insight into the electron transfer, radical oxidation and degradation pathways, *Chem. Eng. J.* 362 (2019) 561–569, <https://doi.org/10.1016/j.cej.2019.01.053>.